

Article

Numerical Investigation of Vortex-Induced Vibration of a Circular Cylinder with Control Rods and Its Multi-Objective Optimization

Zhiyang Hu, Jiaqi Chen, Sen Qu and Xikun Wang * 

Research Center of Fluid Machinery Engineering and Technology, Jiangsu University, Zhenjiang 212013, China
* Correspondence: wangxk@ujs.edu.cn

Abstract: The flow past a 2D circular cylinder with control rods is numerically simulated in the present paper. The suppression effects of the control rods on the vortex-induced vibration (VIV) characteristics of the cylinder are investigated using the overlapping grid method and user defined function. By setting the cylinder's vibration amplitude and drag force coefficient as the expected objective function, a multi-objective optimization is carried out to enhance the suppression performance at different reduced velocities, for which the rod-to-cylinder diameter ratio, gap ratio, incidence angle and reduced velocity are used as design variables. The regression expressions, which are obtained by Box–Behnken design (BBD), are employed in nondominated sorting genetic algorithm II (NSGA-II) to minimize the objectives. It is found that both the optimized vibration amplitude and drag force coefficient exhibit a monotonically decreasing linear trend with the reduced velocity, and as the reduced velocity decreases, the range of the optimized points gradually decreases. Subsequently, the optimized cases are verified by CFD simulations and compared with the original cases. For the samples at the reduced velocity of 4, 5, and 6, the vibration amplitude after optimization decreases by 15.1%, 24.8%, and 21.6%, respectively.

Keywords: cylinder rods body; vortex-induced vibration; Box–Behnken design; multi-objective optimization; nondominated sorting genetic algorithm II



Citation: Hu, Z.; Chen, J.; Qu, S.; Wang, X. Numerical Investigation of Vortex-Induced Vibration of a Circular Cylinder with Control Rods and Its Multi-Objective Optimization. *J. Mar. Sci. Eng.* **2022**, *10*, 1659. <https://doi.org/10.3390/jmse10111659>

Academic Editor:
Masoud Hayatdavoodi

Received: 9 October 2022
Accepted: 1 November 2022
Published: 4 November 2022

Publisher's Note: MDPI stays neutral with regard to jurisdictional claims in published maps and institutional affiliations.



Copyright: © 2022 by the authors. Licensee MDPI, Basel, Switzerland. This article is an open access article distributed under the terms and conditions of the Creative Commons Attribution (CC BY) license (<https://creativecommons.org/licenses/by/4.0/>).

1. Introduction

Vortex-induced vibration (VIV) [1–3] phenomena of cylindrical structures are ubiquitous in offshore structures and marine engineering, such as marine risers [4,5] and petroleum transmission pipelines [6]. When vortex shedding frequency is close to the natural frequency of the bluff body, the resonance phenomenon (lock-in) will occur, which may cause fatigue damage to the structure and seriously threatens its safety. Due to its significance in engineering applications, a large number of numerical simulations [7,8] and experimental studies [9,10] were carried out to explore the underlying mechanism, so as to suppress cylinder VIV.

1.1. Vortex-Induced Vibration Suppression

The research on VIV suppression can be mainly divided into active control and passive control according to whether there is energy injection into the flow field. Compared with active control, passive control is more widely used in engineering practice due to its simple structure and low cost. Till now, a considerable amount of literature on passive control of cylinder VIV was published, which can be roughly classified into three broadest categories. The first category is the splitter plate. Assi et al. [11] studied the VIV suppression using splitter plates in different arrangement forms (fixed or rotating). Their numerical results show that the rotating form can inhibit VIV to some extent and the amplitude of the cylinder with fixed form is positively correlated with the increase in reduced velocity. Hwang et al. [12] experimentally studied the effect of different coverage ratios (Ratio of

cylinder diameter to inlet width) on the VIV of a flexible cylinder at Reynolds numbers ($Re = 2.4 \times 10^3 \sim 7.4 \times 10^3$). It was found that the amplitude of the flexible cylinder in the flow direction can be reduced by 90% and the drag coefficient decreased by 50% when the coverage is less than 50%. Subsequently, Assi et al. [13] studied the mechanism of galloping generated by splitter plates. The results show that the phase angle within the resonance range gradually increases from 0° to 180° with the increase in reduced velocity. This implies that the fluid always did positive work on the cylinder during the whole vibration process and hence increased the vibration amplitude of the cylinder. The second type is bluff body with protrusions. Wu et al. [14] proposed a new traveling-wave wall control strategy for unsteady separation flow of a cylinder. When the downstream part of the cylindrical surface flexibly forms a suitable traveling transverse wave, it will generate waves from inside of each wave slot. The 'Fluid Roller Bearing', composed of a row of vortices, keeps the overall flow under a large unfavorable pressure gradient, thereby eliminating the vortex shedding and reducing the average resistance by up to 85%. Xu et al. [15] employed the traveling wave wall control method to suppress the vibration of a two-degree-of-freedom elastically supported cylinder under a low Reynolds number of $Re = 200$. The results show that a series of small-scale vortices are formed in the traveling wave groove located on the trailing edge of the cylinder. These vortices can effectively control the flow separation and eliminate the oscillations of the wake. As a result, vibration of the cylinder is suppressed. The last type is to modify the shear layers by adding control rods around the cylinder to achieve the suppression effect. This method, widely used in engineering practice, has obvious effects on reducing cylinder vibration. Lesage and Gartshore [16] experimentally studied the force characteristics of the upstream control rod on the downstream cylinder in the range of $Re = 1 \times 10^4 \sim 7 \times 10^4$. It was found that lift and drag forces of the cylinder can be greatly reduced by reasonable spacing control, which shows the spacing ratio is an important parameter in passive control of VIV. Igarashi and Tsutsui [17] also experimentally studied the effect of a single control rod in free flow conditions. The results show that the jet flow induced by the control rod can be adsorbed on the one side of the back edge of the cylinder, which is the fundamental reason to reduce or prevent periodic vortex shedding. Later, Dalton and Yu [18] demonstrated the flow field and force characteristics of the control rod around a cylinder at low Reynolds numbers ($Re = 100, 1000, \text{ and } 3000$) through the experimental and numerical methods. They found that the effect of the control rod is not only related to the spacing, but also to the position. Wu et al. [19] adopted the experimental methods to explore the suppression effect of four control rods on the VIV of a slender riser, and found that increasing the length of the control rods and reducing the spacing can improve the suppression effect. Zhu and Yao [20] studied the effect of the number of control rods (n) on the VIV of an elastically supported cylinder through numerical simulation, and found that the best suppression effect can be achieved when $n = 9$.

1.2. Purpose of This Paper

After decades of research, scholars designed and improved various types of VIV suppression devices. However, it is difficult to balance the suppression performance, practicability, and manufacturing difficulty. Although a number of studies were conducted on the suppression effect of a single control rod and multiple control rods ($n \geq 3$), the research on symmetrically arranged double control rods is still lacking. Moreover, very few studies considered the relationship between multiple variables and objectives (target variables) simultaneously. The paper is organized as follows: Firstly, the SST $k-\omega$ turbulence model based on the Reynolds average Navier–Stokes (RANS) equation is used to simulate VIV characteristics of the cylinder. Then, the Box–Behnken design (BBD) method is employed to obtain the regression expressions of the objectives. Meanwhile, the response surface method based on the computational fluid dynamics (CFD) data are utilized to investigate the interactions between the parameters and the performance. Subsequently, the multi-objective optimization based on nondominated sorting genetic algorithm II (NSGA-II) is carried out to get the Pareto optimal front. Finally, the analyses of the diameter ratio d/D (d

and D are the diameters of the control rods and the cylinder, respectively), the gap ratio G/D (G is the gap distance between the control rods and the cylinder), the incidence angle α and the reduced velocity U_r ($U_r = U/f_n D$, where U is the incoming velocity and f_n is the natural frequency of the cylinder) are presented based on numerical simulations. The obtained results can provide a useful guide for selecting suitable parameters to suppress cylinder VIV.

2. Methodology

2.1. Physical Model

In this paper, the cylinder rods body can freely vibrate in the transverse direction, as shown in Figure 1. The dimensions of the computational domain [21–23] are $40D$ (D is the diameter of the cylinder) in the streamwise direction and $20D$ in the transverse direction, respectively. The center of the cylinder locates at a distance of $10D$ from upstream and two lateral boundaries, yielding a blockage ratio of 5%. Overset mesh technology is employed in the present simulation with a concentric circle of diameter $10D$ specified as the overset region. The diameter, mass ratio and damping ratio of the cylinder are set as 38.1 mm (1.5 inches), 2.4, and 0.0045, respectively, which are the same as those in Khalak and Williamson [24]. The variables in this work are the diameter ratio d/D , the gap ratio G/D , the incidence angle α , and reduced velocity U_r , which range from 0.1 to 0.2, 0.1 to 0.3, 0° to 90° , and 4 to 6 ($2309 \leq Re \leq 3465$), respectively.

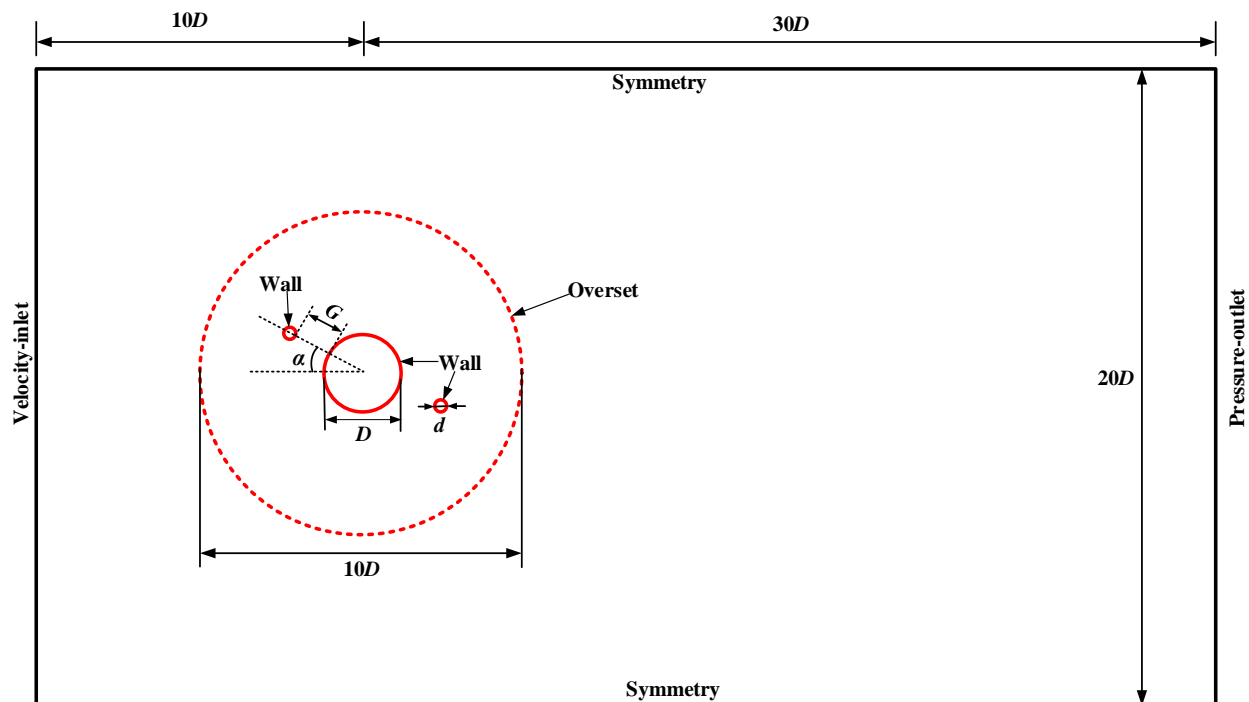


Figure 1. Schematic diagram of the model, computational domain and boundary conditions.

2.2. Governing Equations

The mass conservation, momentum conservation, turbulence, and motion equation are used to describe the flow around the bluff body and the body motion. During the flow process, the periodic vortex shedding would trigger the vibration of the cylinder. Consequently, the fourth order Runge–Kutta method is used to calculate the cylinder motion.

- (1) Mass and momentum conservation equation

The flow past the cylinder rods body is calculated by the two-dimensional unsteady incompressible Navier–Stokes (N-S) equations, including the continuity and momentum equations, expressed as:

$$\frac{\partial u_i}{\partial x_i} = 0 \tag{1}$$

$$\frac{\partial u_i}{\partial t} + u_j \frac{\partial u_i}{\partial x_j} = -\frac{\partial p}{\partial x_i} + \frac{1}{Re} \cdot \frac{\partial}{\partial x_j} \left(\frac{\partial u_i}{\partial x_j} \right) \tag{2}$$

where x_i is the Cartesian coordinate in the i -th direction ($i = 1, 2$), u_i is the velocity component in the direction of x_i , t is the flow time, p is the pressure, ρ is the fluid density, and Re is the Reynolds number based on the diameter of the cylinder and the free-stream velocity.

(2) Turbulence model

Based on the work of Pan et al. [24], the SST k - ω model is suitable for simulating VIV. The turbulence kinetic energy k , and specific rate of dissipation ω , are obtained from the following transport equations:

$$\frac{\partial}{\partial t}(\rho k) + \frac{\partial}{\partial x_i}(\rho k u_i) = \frac{\partial}{\partial x_j} \left[\Gamma_k \frac{\partial k}{\partial x_j} \right] + G_k - Y_k + D_k + S_k \tag{3}$$

$$\frac{\partial}{\partial t}(\rho \omega) + \frac{\partial}{\partial x_i}(\rho \omega u_i) = \frac{\partial}{\partial x_j} \left[\Gamma_\omega \frac{\partial \omega}{\partial x_j} \right] + G_\omega - Y_\omega + D_\omega + S_\omega \tag{4}$$

where: G_k is the generated turbulence kinetic energy, G_ω is the amount generated by its dissipation, Y_k and Y_ω are the dissipations of k and ω due to turbulence, respectively, S_k and S_ω are custom source items, and Γ_k and Γ_ω are the effective diffusion coefficients of k and ω , respectively.

(3) Motion equation

The equation of motion of an elastically mounted cylinder with one degree of freedom in the transverse direction [25] can be expressed by:

$$\ddot{y} + 2\zeta\omega_0\dot{y} + \omega_0^2y = \frac{1}{2m}C_L\rho_fU^2D \tag{5}$$

where ζ is the damping ratio, ω_0 is the circular frequency, and C_L is the lift force coefficient.

Based on the fourth-order Runge–Kutta method [26], the displacement of the cylinder is calculated by,

$$k_1 = f(t_m, y_m) \tag{6}$$

$$k_2 = f\left(t_m + \frac{h}{2}, y_m + \frac{h}{2}k_1\right) \tag{7}$$

$$k_3 = f\left(t_m + \frac{h}{2}, y_m + \frac{h}{2}k_2\right) \tag{8}$$

$$k_4 = f(t_m + h, y_m + hk_3) \tag{9}$$

$$y_{m+1} = y_m + \frac{h}{6}(k_1 + 2k_2 + 2k_3 + k_4) \tag{10}$$

2.3. Simulation Method

Herein the SST k - ω turbulence model based on RANS is used to simulate the cylinder VIV. The coupled algorithm is employed to deal with the pressure–velocity coupling. The convection and momentum term adopted the second-order upwind differencing to accelerate the calculation. Additionally, the second-order upwind scheme is used for turbulent kinetic energy and specific dissipation rate. The velocity inlet boundary condition is given at the inlet with the turbulent intensity setting as 5.0%. The outlet is set as pressure

outlet boundary conditions. The surfaces of the cylinder rods body are specified as a no-slip wall boundary condition. In order to avoid the effect of lateral boundaries on the flow field, symmetry boundary conditions are applied. Based on the overlapping grid method, the motion of the cylinder is written and accessed through user-defined function (UDF) macro commands by the software Fluent. The pressure-based non-steady-state format is used for calculation with a time step $\Delta t = 0.001$ s. The maximum number of iterations is set to 200, and the convergence criterion is set to the residual less than 10^{-6} to ensure the convergence and accuracy of the calculation.

2.4. Validity of Numerical Scheme

2.4.1. Meshing and Mesh Independence Check

The computational flow domain is meshed using integrated computer engineering and manufacturing (ICEM). Figure 2 shows the overall mesh of the computational domain and the enlarged views around the cylinder rods body. The mesh is composed of components of grids from the background section and foreground part. The background mesh, marked in black, is meshed by structured grids. The foreground mesh, marked in red, is divided with the gradient form based on structured cells, which remain ideal for calculation results. A more refined mesh is also required near the walls of the cylinder rods body to capture the flow characteristics. The boundary layer on the cylinder surface is laminar. In this region, the minimum grid size is 0.204 mm, $U_r = 5$ ($Re = 2889$), corresponding to dimensionless wall distance $y^+ \sim 1$ ($y^+ = U_\tau \Delta_1 / \nu$, where U_τ is the wall shear velocity, Δ_1 is the first layer mesh thickness, and ν is the kinematic viscosity of the fluid). Nearby the overset boundary, the difference in the grid size between background and foreground interfaces is small enough to ensure the accuracy of the data exchange.

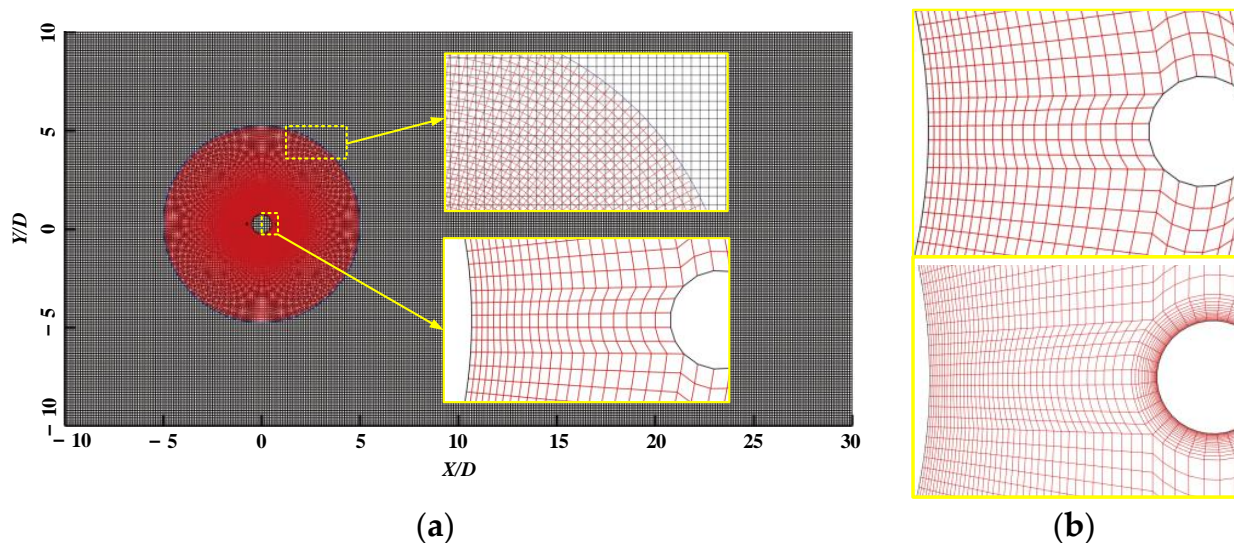


Figure 2. (a) Overall grid in the computational domain and local mesh near the overset boundary and structure surface ($d/D = 0.1$, $G/D = 0.2$, $\alpha = 0^\circ$, and $U_r = 5$) and (b) mesh near the control rods.

The computational accuracy and convergence speed of a numerical simulation depends to a large extent on the density of grids. Therefore, it is important to verify the mesh independence by using different sets of meshes. The obtained vibration amplitude and drag force of the cylinder with the five sets of grids (M1–M5) are shown in Table 1. It can be seen that the relative difference in the normalized vibration amplitude A^* ($A^* = A/D$, where A is the amplitude of the cylinder vibration in transverse direction) between M4 and M5 is less than 0.2%. Additionally, the relative error in drag force coefficient C_D ($C_D = F_D / 0.5\rho U^2 D$, where F_D is the drag force of the cylinder, ρ is the density of the fluid, and U is the incoming flow speed) between M4 and M5 is less than 0.5%. Meanwhile, the M4 is also tested for encryption near the lever, as shown in Figure 2b. The results show that the difference

between A^* and C_D of the two sets of grids is 1.52% and 0.98%, respectively. Therefore, based on a compromise between the computational accuracy and cost, the mesh M4 will be used in the subsequent numerical simulations.

Table 1. Mesh independence test results.

Mesh	Number of Elements	A^*	C_D
M1	24132	0.724	2.443
M2	36706	0.815	2.612
M3	49380	0.981	2.946
M4	70236	1.013	3.041
M5	107112	1.017	3.062

2.4.2. Numerical Validation

In this section, validation studies are conducted by comparing the numerically obtained vibration amplitude A^* with the experimental data in Khalak and Williamson [27], as shown in Figure 3. Two sets of data are in good agreement and the maximum relative error is less than 7%, which proves the validity and accuracy of the mathematical model and UDF adopted in this paper. Meanwhile, the drag force coefficients C_D at $U_r = 4, 5,$ and 6 are compared with Khalak and Williamson [23], with a maximum deviation of no more than 5%.

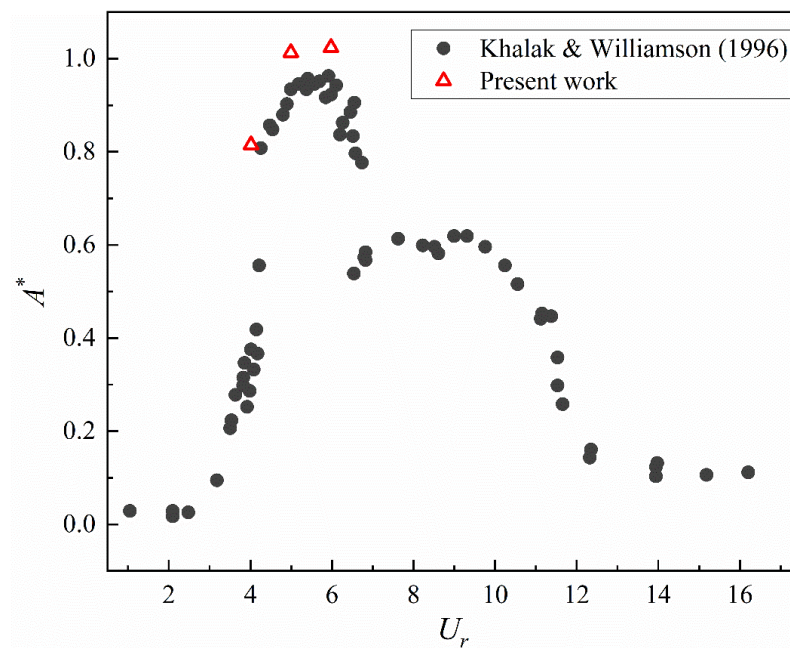


Figure 3. Comparison of the obtained vibration amplitude A^* with the experimental data in Khalak and Williamson [27].

2.5. Response Surface Methodology

The response surface method (RSM) is based on a series of statistical and mathematical methods to construct a response surface model between variables and objectives. The central composite design (CCD) method and the Box–Behnken design (BBD) method [28] are usually used for the design of experimental or numerical simulation. Compared with the CCD method, the BBD method is adopted in this paper due to its fewer cases and lower computational cost. BBD design of simulations with four variables and two objectives were constructed by Design Expert10 software [29]. Table 2 presents the variation ranges and the limits of the four variables. Additionally, the boundaries of the design space are defined as three levels, which represent the basic rule for the selection of design cases. In total,

29 simulation cases (including 5 repeated cases at the center position) obtained by the BBD method and the corresponding numerical results are shown in Table 3.

Table 2. The values of four factors and three levels.

Design Parameters	Level		
	−1	0	1
Diameter ratio (d/D)	0.1	0.15	0.2
Gap ratio (G/D)	0.1	0.2	0.3
Incidence angle (α , °)	0	15	30
Reduced velocity (U_r)	4	5	6

Table 3. Simulation scheme by BBD and the corresponding CFD results.

Run No.	Cylinder Rods Body Parameters				CFD Results	
	d/D	G/D	α (°)	U_r	A^*	C_D
1	0.15	0.1	15	6	0.751	1.687
2	0.15	0.3	30	5	0.809	2.429
3	0.2	0.3	15	5	0.758	1.934
4	0.1	0.2	0	5	0.705	2.178
5	0.1	0.3	15	5	0.761	2.296
6	0.15	0.2	30	6	0.759	1.833
7	0.15	0.3	15	6	0.831	2.043
8	0.1	0.2	15	4	0.701	2.527
9	0.1	0.2	30	5	0.684	2.326
10	0.15	0.2	15	5	0.698	2.045
11	0.2	0.1	15	5	0.872	1.678
12	0.15	0.1	0	5	0.895	1.892
13	0.2	0.2	15	4	0.767	1.754
14	0.15	0.3	15	4	0.651	1.845
15	0.15	0.1	15	4	0.692	1.401
16	0.15	0.2	15	5	0.698	2.045
17	0.15	0.2	15	5	0.698	2.045
18	0.2	0.2	30	5	0.739	1.54
19	0.15	0.2	15	5	0.698	2.045
20	0.2	0.2	0	5	0.908	1.892
21	0.15	0.2	15	5	0.698	2.045
22	0.1	0.1	15	5	0.89	2.008
23	0.2	0.2	15	6	0.87	1.871
24	0.15	0.2	0	6	0.93	1.904
25	0.15	0.2	30	4	0.697	1.914
26	0.15	0.2	0	4	0.691	2.335
27	0.15	0.3	0	5	0.861	1.927
28	0.15	0.1	30	5	0.715	1.64
29	0.1	0.2	15	6	0.741	1.931

2.6. Genetic Algorithms

The multi-objective optimization is more complicated than the single-objective counterpart because of synergistic effects between different variables. Meanwhile, the relationship between each variable and the multiple-objective functions is also inconsistent. Therefore, the genetic algorithm based on the biological evaluation mechanism, which is widely used in multi-objective optimization problems, is adopted in the present study. It generates the next-generation algorithm by selection, crossover, and mutation, so linear or nonlinear objective functions can be optimized [30]. Different from the first-generation algorithm, NSGA-II [31] proposes new concepts of fast nondominated sorting and crowded sorting. The Pareto optimal solution generated by the new concepts is used to perform the next iterative calculation, and some proposals will be rejected during the crowded sorting process [32].

3. Results and Discussion

3.1. Multi-Objective Optimization

The results obtained by the BBD method will further analyze the relationship between the variables and the objectives by response surface method and obtain the regression equation. Subsequently, the regression equation will be multi-objective optimization through NSGA-II, which is implemented by a program written in software MATLAB. The corresponding results and further analysis are presented as follows.

3.1.1. Response Surface Analysis

For problems with multiple influencing variables and a mutual influence relationship between the variables, it is usually expressed in the form of a quadratic polynomial. The RSM adopts using quadratic polynomials to fit the response relationship between each variable and the objective. The quadratic polynomial is also called regression equation in the response surface analysis. Based on the data in Table 3, the regression equations, which are obtained by the software Design Expert 10 for the objectives, are as follows:

$$A^* = 0.9325 - 6.785 \cdot d/D - 2.63833 \cdot G/D + 0.00742778 \cdot \alpha + 0.1155 \cdot U_r + 0.75 \cdot d/D \cdot G/D - 0.049333 \cdot d/D \cdot \alpha + 0.315 \cdot d/D \cdot U_r + 0.021333 \cdot G/D \cdot \alpha + 0.0775 \cdot G/D \cdot U_r - 0.00295 \cdot \alpha \cdot U_r + 21.73333 \cdot d/D^2 + 4.43333 \cdot G/D^2 + 0.000239815 \cdot \alpha^2 - 0.00629167 \cdot U_r^2 \quad (11)$$

$$C_D = 2.83221 - 21.73333 \cdot d/D + 6.23667 \cdot G/D - 0.032361 \cdot \alpha + 0.292 \cdot U_r - 1.6 \cdot d/D \cdot G/D - 0.16667 \cdot d/D \cdot \alpha + 3.565 \cdot d/D \cdot U_r + 0.12567 \cdot G/D \cdot \alpha - 0.22 \cdot G/D \cdot U_r + 0.00583333 \cdot \alpha \cdot U_r + 8 \cdot d/D^2 - 12.4375 \cdot G/D^2 + 0.0000194444 \cdot \alpha^2 - 0.09125 \cdot U_r^2 \quad (12)$$

Figure 4 shows the fitting situation of the two objectives (A^* and C_D) in this study obtained by the CFD simulations using the methods of BBD and RSM. It can be seen that the predicted and actual values fit well. Another indicator for evaluating RSM is multiple correlation coefficient, R^2 , whose value ranges from 0 to 1. The larger value of R^2 , the better the fit of the response surface model. The maximum values of R^2 for A^* and C_D are 0.9047 and 0.9529, respectively, indicating that the regression equation model is very reliable. In addition, Table 4 shows the variance analysis results of the response model for the objectives to verify the scientific and statistical significance of this research. For any variable, the larger F value and the smaller p value imply a higher impact on the objective, or a better statistical performance. The p values for A^* and C_D are less than 0.38 and 0.089, respectively. The diameter ratio and the reduced velocity also achieve their respective minimum p values. The results show that the statistical results of A^* are more significant than C_D , which also indicates that the response of the four parameters to A^* is stronger in the parameter ranges.

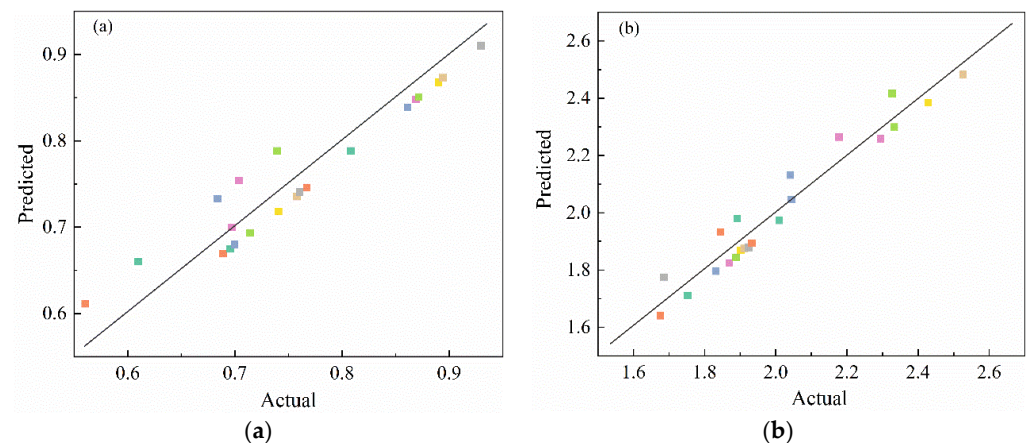


Figure 4. Fitting situation of two objectives: (a) A^* and (b) C_D .

Table 4. Variance analysis of A^* and C_D .

Source	Vibration Amplitude			Drag Force Coefficient		
	Sum of Squares	F-Value	p-Value	Sum of Squares	F-Value	p-Value
d/D	9.506×10^{-3}	2.13	0.1952	0.17	11.86	0.0137
G/D	4.16×10^{-3}	0.93	0.3721	0.16	10.94	0.0163
α	6.806×10^{-3}	1.52	0.2635	0.061	4.14	0.0882
U_r	0.023	5.06	0.0654	0.066	4.48	0.0768

The response surface of the cylinder rods body makes the relationship between the parameters and performance (variables and objectives) visualized, facilitating the analysis of the influence of parameter changes. Figure 5 shows the response relationship between the objectives (A^* and C_D) and any two of the three variables (d/D , G/D , and α). It can be seen from Figure 5a–c that the extreme values of A^* are obtained when d/D , G/D , and α take the median values. Specifically, Figure 5a shows the response surface of A^* to d/D and G/D . At this time, α and U_r take the median values of the design range. It can be concluded that when G/D takes the upper or lower limit, the response relationship of A^* to d/D is relatively large. At $G/D = 0.1$, A^* achieves the minimum value when d/D is near the median value. At $G/D = 0.3$, A^* increases first and then decreases with the increase in d/D . This is because when G/D is small, the shielding phenomenon between the cylinder and the control rods is prominent. As G/D increases, the effect of the control rods on the flow field around the cylinder becomes more significant. The trends displayed in Figure 5 (b) and (c) are similar: when α is constant, A^* first increases and then decreases with the increase in d/D and G/D . The numerical result is consistent with the study of Sakamoto and Haniu [33] on a single control rod. Figure 5d–f shows the response surfaces of C_D to d/D and G/D and α , respectively. The minimum value of C_D is obtained when d/D is extremely small or large. This is because the control rods contribute a larger portion of the drag force of the cylinder when the value of d/D is large. Meanwhile, the control rods also cause the greatest disturbance to the flow field of the cylinder when $G/D = 0.3$. Additionally, C_D shows a monotonically increasing trend with the increase in α . These phenomena are also consistent with the findings of Zhao et al. [34]. In summary, since the relationships between variables and objectives are distinctive, which causes each variable = produces different effects on the objectives. Randomly combined variables will have a more complex effect on the objectives.

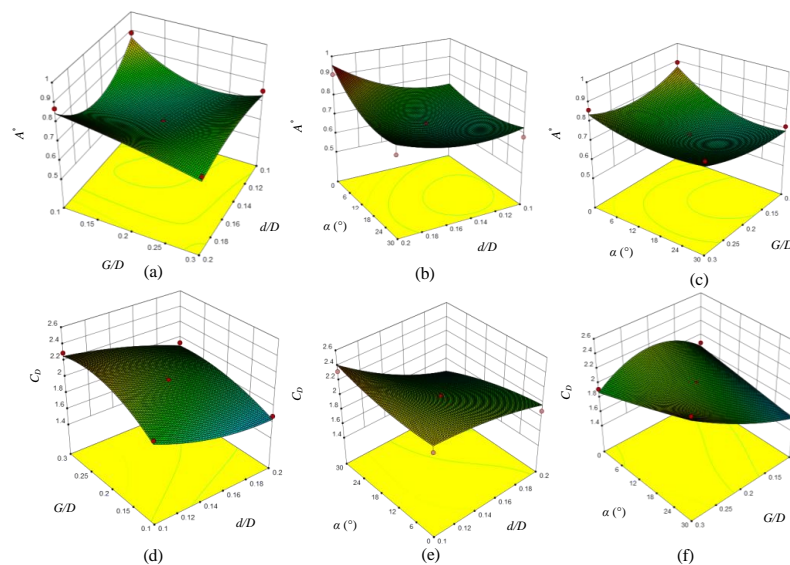


Figure 5. Response surfaces of A^* (top row) and C_D (bottom row) with reference to d/D , G/D , α . (a), (d) G/D and α ; (b,e) α and d/D ; (c,f) α and G/D .

3.1.2. Optimization Using NSGA-II

Based on the response surface model, this paper uses NSGA-II to carry out multi-objective optimization of the cylinder rods body, and obtains the optimal design set. The setting parameters of the algorithm are as follows: the initial population size is 100, the number of iterations is 500, the number of objectives is 2, the number of decision variables (also named dimensions) is 4, the individual crossover probability is 0.9, and the individual mutation probability is 0.5. When optimizing the design parameters d/D , G/D , α and U_r , the minimum values of the two objectives, A^* and C_D , need to be considered simultaneously. The optimization problem can also be expressed as the following form:

$$\left\{ \begin{array}{ll} \text{minimize} & A^* = Y_1(d/D, G/D, \alpha, U_r) \\ \text{minimize} & C_D = Y_2(d/D, G/D, \alpha, U_r) \\ & 0.1 \leq d/D \leq 0.2 \\ & 0.1 \leq G/D \leq 0.3 \\ & 0^\circ \leq \alpha \leq 30^\circ \\ & 4 \leq U_r \leq 6 \end{array} \right. \quad (13)$$

The Pareto results obtained by multi-objective optimization are shown in Figure 6. Figure 6a presents the Pareto front composed of the optimal solution obtained by NSGA-II and the original data obtained by the BBD method. It can be seen that the obtained C_D - A^* curve shows a monotonic relationship, that is, C_D decreases with the increases in A^* . The original results obtained by BBD, however, do not show any apparent variation trend. This illustrates the effectiveness of multi-objective optimization. Figure 6b shows the distribution of each design parameter of the optimized solution collection. The change in each parameter is small when $A^* \geq 0.69$, which means that the variables will eventually become stable in their respective optimization intervals. At $A^* \leq 0.69$, on the contrary, all variables exhibit a certain linear or fluctuating relationship. The curves of d/D and α show a monotonically increasing trend with increasing A^* , whereas that of G/D decreases monotonically with increasing A^* . The calculated results mentioned above are also consistent with the research on reflecting the reliability of the optimization in Sakamoto and Haniu [33]. The change in U_r is not obvious, except for a narrow range around $U_r = 4$. This coincides with the transition range between the initial branch and the upper branch.

The reduced velocity is a very important parameter for VIV. From the analysis of variance and response surface analysis, it can be seen that the change in reduced velocity has a very significant effect on the performance of the cylinder rods body. To achieve different target values (objectives), simply changing the reduced velocity will weaken the effect of other parameters (variables). Therefore, it is necessary to give the design parameter combination according to different reduced velocities. The results of multi-objective optimization based on NSGA-II for $U_r = 4, 5$, and 6 are provided in Figure 7. It can be seen that for the Pareto solution sets, C_D exclusively displays a monotonically decreasing trend with the increase in A^* . Moreover, the variation range of A^* and C_D of the multi-objective optimization design point is decreased with increasing U_r . Compared with $U_r = 4$, the decreasing trend of the solution set distribution for $U_r = 5$ and 6 gradually slows down with the increase in A^* . This means that it is easier for C_D to reach the optimal extreme value when U_r is increased. Meanwhile, the corresponding design parameters are given in Figure 8. Figure 8a shows that both d/D and α increase monotonically with A^* , but decrease monotonically for the case of $U_r = 4$. It is worth noting that at $A^* \geq 0.71$, G/D and α are concentrated around 0.1 and 30° , respectively. This implies that when G/D is small or α is large, it is reasonable to choose a smaller value of d/D for optimization. Figure 8b shows the optimized design obtained by NSGA-II for $U_r = 5$. Under the circumstance of $A^* \geq 0.72$, G/D and α are stable around 0.1 and 30° , respectively, whereas d/D increases with A^* . This trend is more obvious in the cases of $U_r = 6$ as shown in Figure 8c, which shows that A^* can be greatly reduced by reducing d/D at a higher reduced velocity. This also confirms

the phenomenon in Figure 7 that the range of the design point gradually decreases with the increase in U_r . In summary, the above multi-objective optimization results explain the evaluation trend of the design parameters of the cylinder rods body under specific reduced velocity. The designer can propose some solution to optimize the design according to the value of U_r .

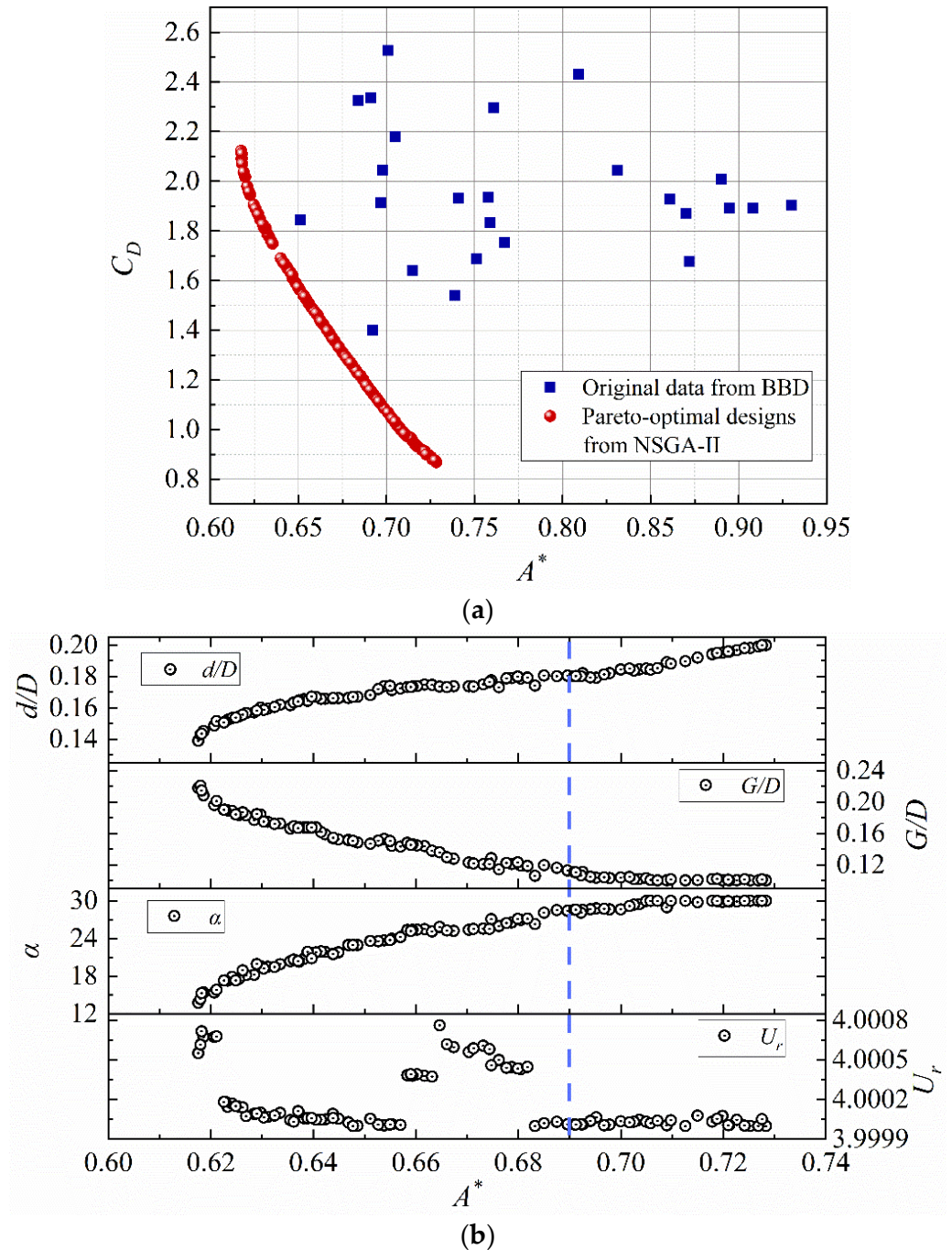


Figure 6. Multi-objective Pareto results: (a) Pareto front and (b) designs of Pareto front points.

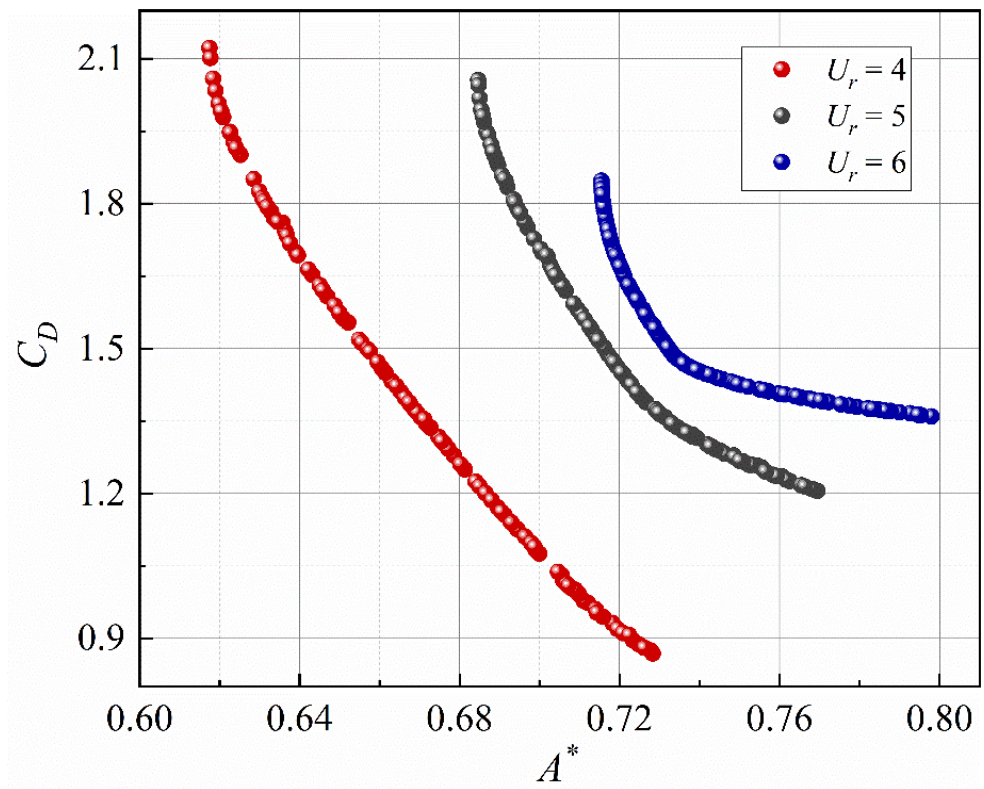


Figure 7. Pareto front at different reduced velocities.

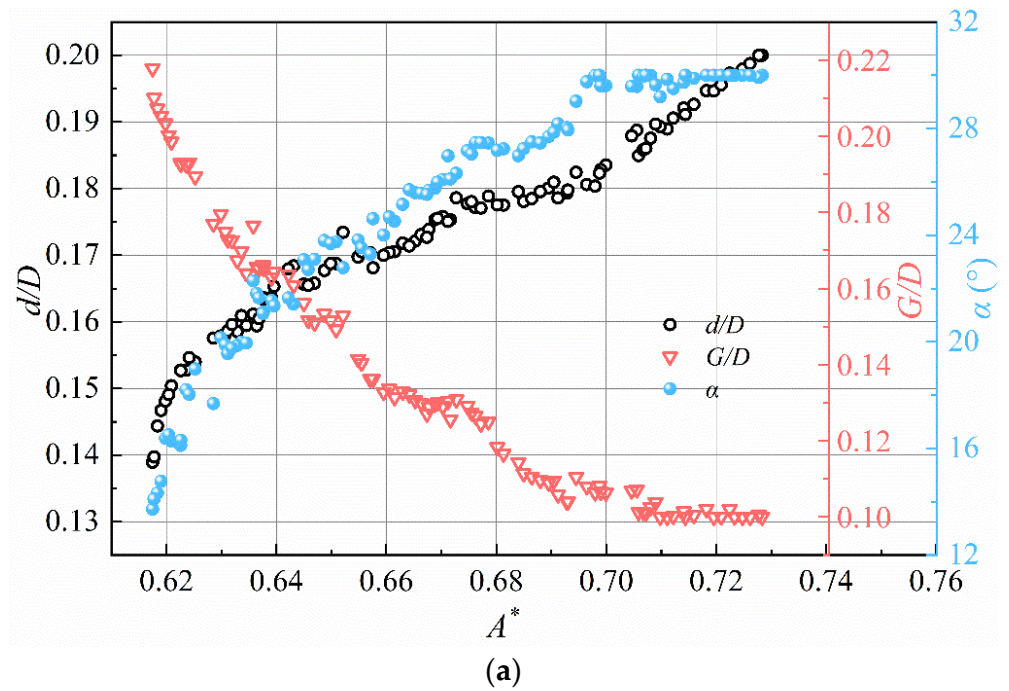


Figure 8. Cont.

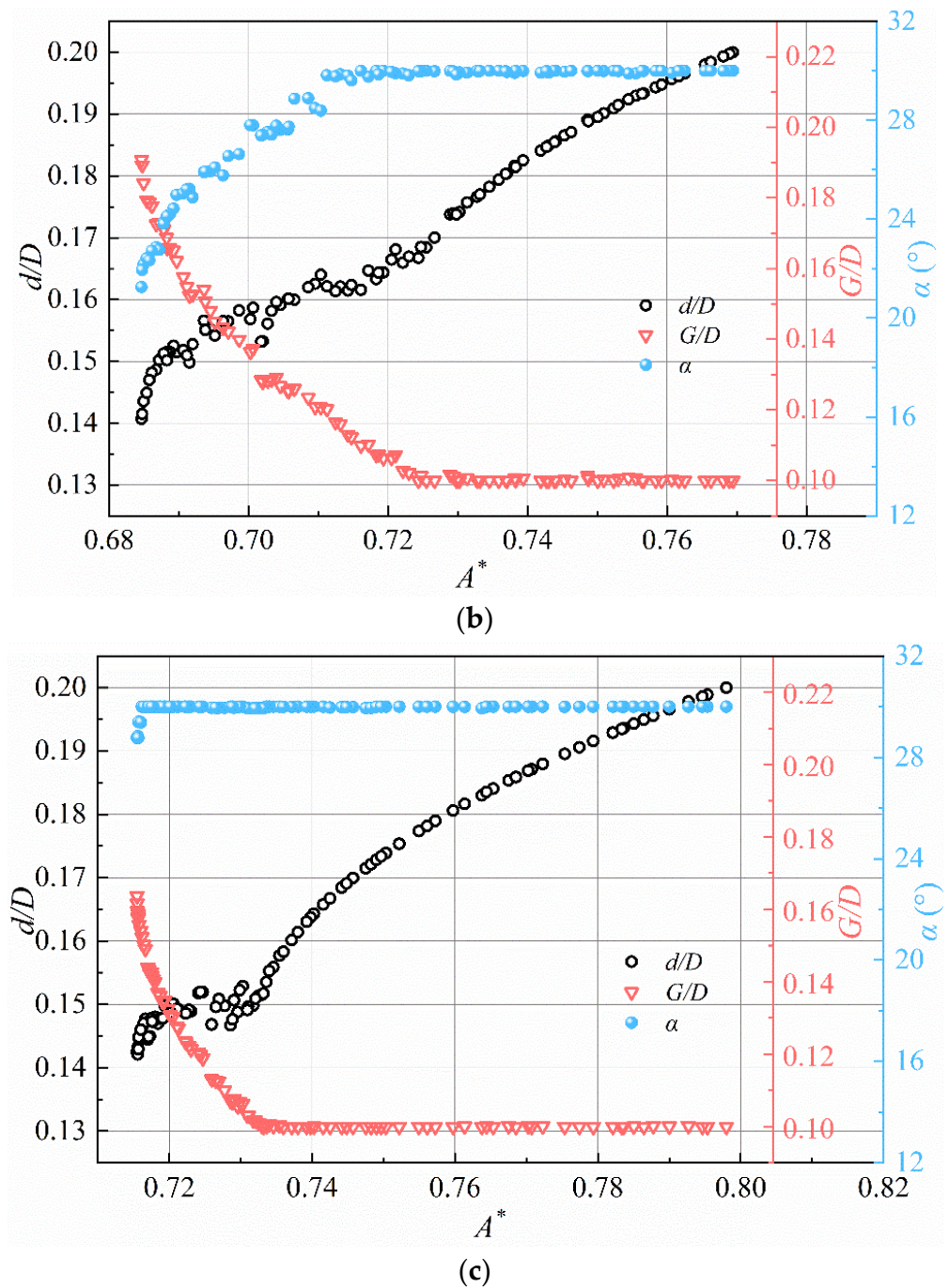


Figure 8. Optimal designs at different reduced velocities. (a) $U_r = 4$; (b) $U_r = 5$; and (c) $U_r = 6$.

3.2. Verification of Optimization Results and Comparison Flow Fields

The multi-objective optimization based on NSGA-II gives a series of design points and the corresponding performance prediction results. Comparison between the performance before and after optimization of the cylinder rods body and analysis of the flow field are presented as follows.

3.2.1. Comparison and Verification

In order to quantitatively assess the effect of multi-objective optimization, the optimized results are compared with the original designs. The samples must have a certain good performance; otherwise, the significance of the comparative study will be weakened. Table 5 shows the structure design of the cylinder rods body before and after optimization

at different reduced velocities, as well as the NSGA-II and CFD numerical simulation results of the corresponding samples. It can be concluded that the optimized design points usually take larger G/D and α when d/D is similar. Additionally, when the value of α before and after optimization is similar, a larger d/D is obtained, which also shows that NSGA-II achieves the optimal value among the two objectives. For the samples of $U_r = 4, 5,$ and 6 , the vibration amplitude after optimization is reduced by 15.1%, 24.8%, and 21.6%, respectively. Additionally, CFD simulations were carried out on the predicted optimal values to verify the accuracy and credibility of the optimization. As shown in Table 5, the predicted performance from NSGA-II does not have a large deviation from the CFD results.

Table 5. Simulation results before and after multi-objective optimization.

Run.	U_r	d/D	G/D	α (°)	NSGA-II		CFD Results		Deviation (%)		
					A^*	C_D	A^*	C_D	A^*	C_D	
1	Before	4	0.2	0.2	15	/	/	0.767	1.754	/	/
2	After	4	0.18	0.13	27.2	0.674	1.317	0.651 (↓ 15.1%)	1.248	3.4%	5.2%
3	Before	5	0.1	0.1	15	/	/	0.89	2.008	/	/
4	After	5	0.15	0.17	24.1	0.688	1.907	0.669 (↓ 24.8%)	1.846	2.7%	3.2%
5	Before	6	0.15	0.2	0	/	/	0.93	1.904	/	/
6	After	6	0.17	0.1	30	0.742	1.448	0.729 (↓ 21.6%)	1.426	1.8%	3%

3.2.2. Flow Patterns before and after Optimization

The above comparative analysis reflects the difference between the design points and the performance (variables and objectives) of the cylinder rods body. In fact, the change in objectives is actually due to the change in flow characteristics. Flow field differences are inherently related to performance changes, so analysis of the flow field is necessary. Figure 9 shows the instantaneous vorticity fields around the cylinder rods body before and after multi-objective optimization, which are obviously different from that of the single cylinder in Morse and Williamson [35]. It can be concluded that the influence of the control rods after optimization on the vortex shedding of the cylinder is significantly strengthened. Additionally, the bearing of the drag force of the upstream control rod to the cylinder will be increased with the increase in d/D and α under the same G/D , which makes the downstream control rod have a better suppression effect of vortex shedding from the cylinder. Figure 10 shows the corresponding mean streamlines for different cases, from which one can more intuitively appreciate the flow patterns around the cylinder rods body. It can be seen that the streamlines after optimization are evidently smoother than the corresponding counterparts before optimization, which also verifies the optimization of C_D . The influence of the control rod on the flow field at the rear of the cylinder is the same as in Figure 9, which also proves the reduction in A^* . In summary, the comparative analysis of the flow field more intuitively shows the flow field change in the cylinder rods body after multi-objective optimization, illustrating the connection between the flow pattern and the flow parameters (variables and objectives).

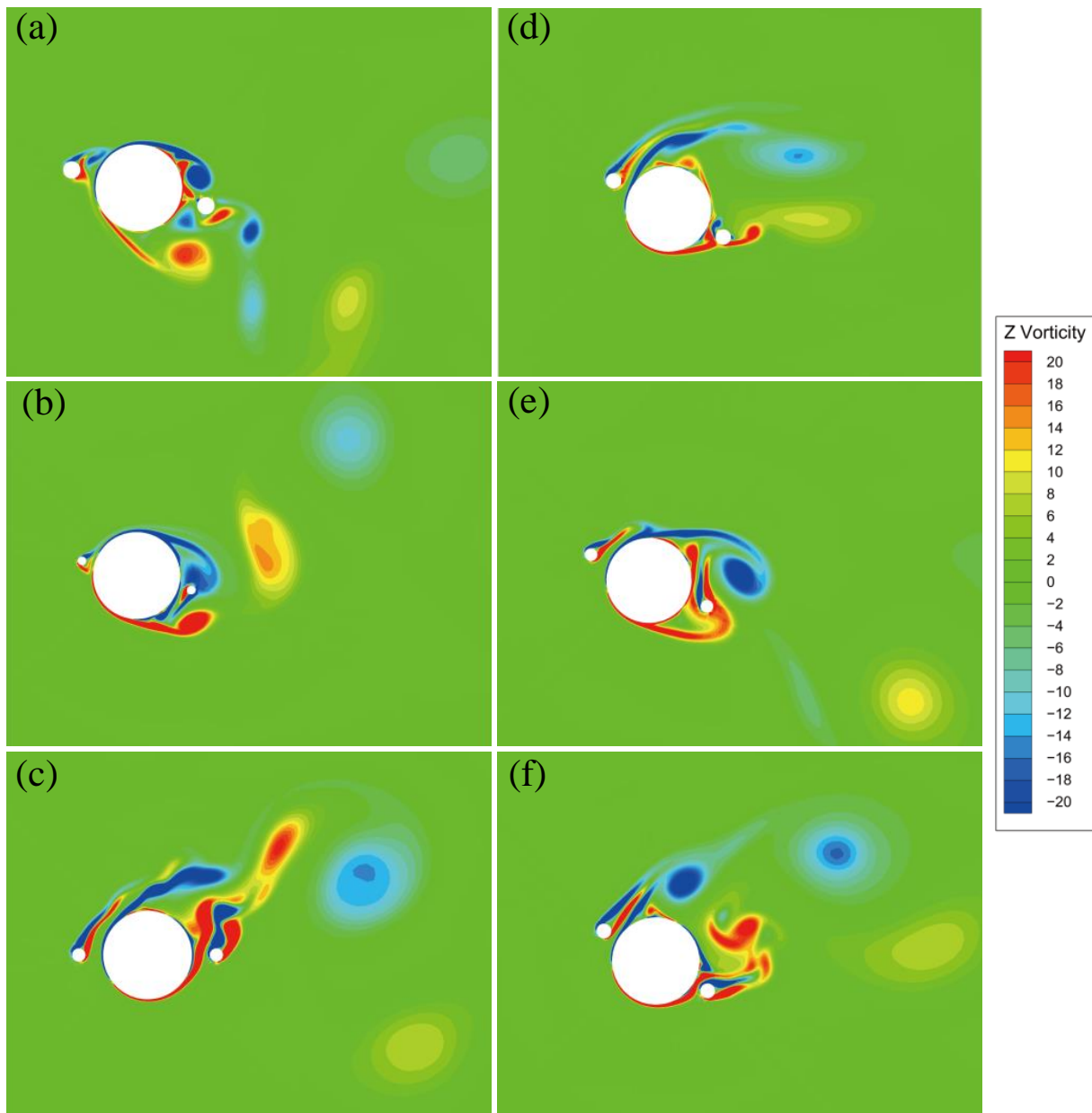


Figure 9. Instantaneous vorticity field before (left column) and after (right column) multi-objective optimization at $U_r = 4$ (a,d), 5 (b,e), and 6 (c,f).

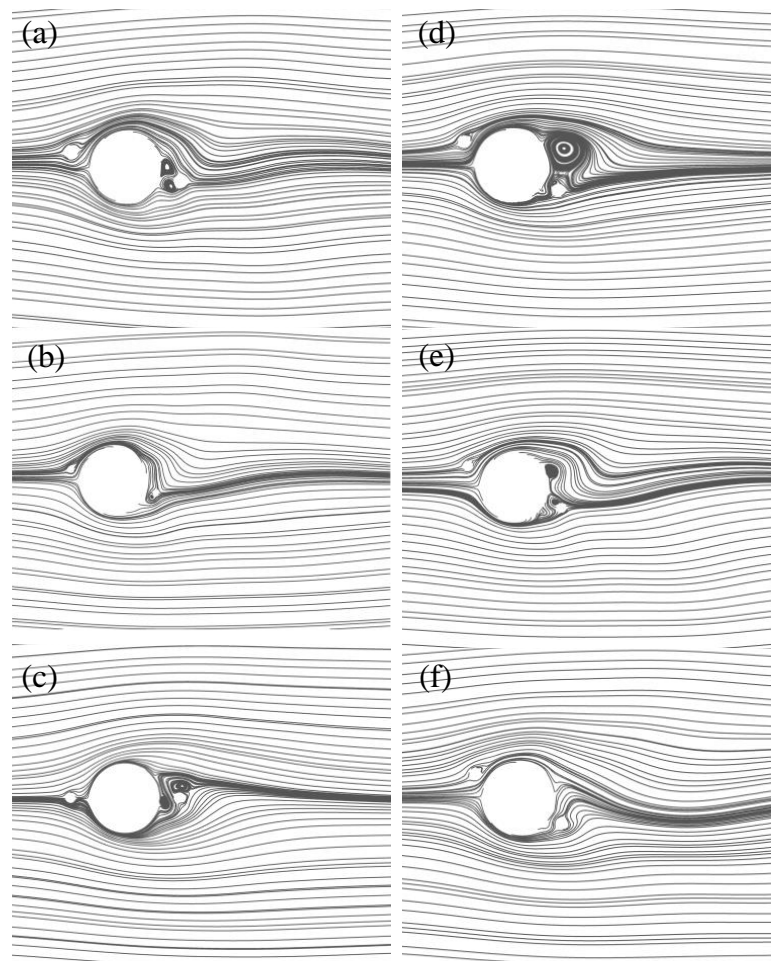


Figure 10. Mean streamlines before (left column) and after (right column) multi-objective optimization at $U_r = 4$ (a,d), 5 (b,e), and 6 (c,f).

4. Conclusions

The vortex-induced vibration (VIV) of a circular cylinder with a pair of symmetrically arranged control rods is a complex multi-parameter problem, which involves many parameters, including diameter ratio, gap ratio, incidence angle, and reduced velocity. In this paper, the influence of different variables on the objectives is analyzed by the response surface method (RSM). Then, the vibration amplitude and drag force coefficient of the cylinder are optimized by the NSGA-II. Finally, the original cases and the optimized cases under different reduced velocities are compared and analyzed. The main conclusive remarks are as follows:

- (1) The response surfaces show that there is an extreme value of A^* under different combinations of variables. Among them, d/D shows a different synergistic effect from the other two variables. When $d/D = 0.1$, G/D achieves the minimum value of A^* at the median value; when $d/D = 0.3$, G/D achieves the minimum value of A^* at the upper limit and displays a monotonically decreasing trend. Unlike A^* , the extreme point of C_D occurs in the case of larger d/D and α , and small G/D .
- (2) The multi-objective optimization based on NSGA-II gives a series of Pareto optimal solutions for different reduced velocities ($U_r = 4, 5$, and 6). In general, the optimal design points of d/D all form a monotonically increasing relationship with A^* , irrespective of reduced velocity. However, G/D and α will reach a stable design point with the increase in A^* . Compared with the original cases, the values of A^* after optimization are reduced by 15.1%, 24.8%, and 21.6% for $U_r = 4, 5$, and 6, respectively.

- (3) After the multi-objective optimization, the design variables d/D , G/D , and α reach the design points, and the objectives A^* and C_D also achieve the Pareto front at different U_r . These results can provide a useful reference for the optimal design of the cylinder rods body to suppress VIV.

Author Contributions: Conceptualization, Z.H. and X.W.; methodology, Z.H. and J.C.; software, Z.H. and S.Q.; validation, Z.H., J.C. and S.Q.; formal analysis, X.W.; investigation, Z.H.; resources, J.C.; data curation, Z.H. and S.Q.; writing—original draft preparation, Z.H.; writing—review and editing, J.C., S.Q. and X.W.; visualization, S.Q.; supervision, X.W.; project administration, X.W. All authors have read and agreed to the published version of the manuscript.

Funding: This research was funded by the National Natural Science Foundation of China (Grant number 52079057).

Institutional Review Board Statement: Not applicable.

Informed Consent Statement: Not applicable.

Data Availability Statement: Data will be available upon request.

Conflicts of Interest: The authors declare no conflict of interest.

References

1. Yayli, M. Axial vibration analysis of a Rayleigh nanorod with deformable boundaries. *Microsyst. Technol.* **2020**, *26*, 2661–2671. [[CrossRef](#)]
2. Yayli, M. Torsional vibration analysis of nanorods with elastic torsional restraints using non-local elasticity theory. *Micro Nano Lett.* **2018**, *13*, 595–599. [[CrossRef](#)]
3. Yayli, M. Free vibration analysis of a rotationally restrained (FG) nanotube. *Microsyst. Technol.* **2019**, *25*, 3723–3734. [[CrossRef](#)]
4. Wang, W.Q.; Yu, Z.F.; Gao, Y.; Luo, J.L.; Cao, W.Z. Study on the hydrodynamic characteristics of a marine riser under periodic pulsation disturbance. *Ocean. Eng.* **2021**, *223*, 108696. [[CrossRef](#)]
5. Wang, D.; Hao, Z.F.; Pavloskaia, E.; Wiercigroch, M. Bifurcation analysis of vortex-induced vibration of low-dimensional models of marine risers. *Nonlinear Dyn.* **2021**, *106*, 147–167. [[CrossRef](#)]
6. Yan, S.T.; Zhu, Y.F.; Jin, Z.J.; Ye, H. Buckle propagation analysis of deep-water petroleum transmission pipelines with axial tension. *Adv. Mater. Res.* **2014**, *1008–1009*, 1134–1143. [[CrossRef](#)]
7. Faucher, V.; Ricciardi, G.; Boccaccio, R.; Cruz, K.; Lohez, T.; Clément, S.A. Numerical implementation and validation of a porous approach for fluid-structure interaction applied to pressurized water reactors fuel assemblies under axial water flow and dynamic excitation. *Int. J. Numer. Methods Eng.* **2021**, *122*, 2417–2445. [[CrossRef](#)]
8. Mao, X.R.; Zhang, L.; Hu, D.J.; Ding, L. Flow induced motion of an elastically mounted trapezoid cylinder with different rear edges at high Reynolds numbers. *Fluid Dyn. Res.* **2019**, *51*, 025509. [[CrossRef](#)]
9. Wang, X.K.; Wang, C.; Li, Y.L.; Tan, S.K. Flow patterns of a low mass-damping cylinder undergoing vortex-induced vibration: Transition from initial branch and upper branch. *Appl. Ocean. Res.* **2017**, *62*, 89–99. [[CrossRef](#)]
10. Wang, X.K.; Hao, Z.; Tan, S.K. Vortex-induced vibrations of a neutrally buoyant circular cylinder near a plane wall. *J. Fluids Struct.* **2013**, *39*, 188–204. [[CrossRef](#)]
11. Assi, G.R.S.; Bearman, P.W.; Kitney, N. Low drag solutions for suppressing vortex-induced vibration of circular cylinders. *J. Fluids Struct.* **2009**, *25*, 666–685. [[CrossRef](#)]
12. Hwang, J.Y.; Yang, K.S.; Sun, S.H. Reduction of flow-induced forces on circular cylinder using a detached splitter plate. *Phys. Fluids* **2003**, *15*, 2433–2436. [[CrossRef](#)]
13. Assi, G.R.S.; Bearman, P.W.; Kitney, N. Transverse galloping of circular cylinders fitted with solid and slotted splitter plates. *J. Fluids Struct.* **2015**, *25*, 666–675. [[CrossRef](#)]
14. Wu, C.J.; Wang, L.; Wu, J.Z. Suppression of the von Karman vortex street behind a circular cylinder by travelling wave generated by a flexible surface. *J. Fluid Mech.* **2007**, *574*, 365–391. [[CrossRef](#)]
15. Xu, F.; Chen, W.-L.; Xiao, Y.-Q.; Li, H.; Ou, J.-P. Numerical study on the suppression of the vortex-induced vibration of an elastically mounted cylinder by a traveling wave wall. *J. Fluids Struct.* **2014**, *44*, 389–447. [[CrossRef](#)]
16. Lesage, F.; Gartshore, I.S. A method of reducing drag and fluctuating side force on bluff bodies. *J. Wind. Eng. Ind. Aerodyn.* **1987**, *25*, 229–245. [[CrossRef](#)]
17. Igarashi, T.; Tsutsui, T. Flow control around a circular cylinder by a new method (2nd report, fluids forces acting on the cylinder). *Trans. JSME* **1989**, *55*, 708–714. [[CrossRef](#)]
18. Dalton, C.; Xu, Y. The suppression of lift on a circular cylinder due to vortex shedding at moderate Reynolds numbers. *J. Fluids Struct.* **2001**, *15*, 617–628. [[CrossRef](#)]
19. Wu, H.; Sun, D.; Lu, L.; Teng, B.; Tang, G.; Song, J. Experimental investigation on the suppression of vortex-induced vibration of long flexible riser by multiple control rods. *J. Fluid Struct.* **2012**, *30*, 115–132. [[CrossRef](#)]

20. Zhu, H.J.; Yao, J. Numerical evaluation of passive control of VIV by small control rods. *Appl. Ocean. Res.* **2015**, *51*, 93–116. [[CrossRef](#)]
21. Ong, M.C.; Utnes, T.; Holmedal, L.E.; Myrhaug, D.; Pettersen, B. Numerical simulation of flow around a smooth circular cylinder at very high Reynolds numbers. *Mar. Struct.* **2009**, *22*, 142–153. [[CrossRef](#)]
22. Dey, P.; Das, A.K. Prediction and optimization of unsteady forced convection around a rounded cornered square cylinder in the range of Re. *Neural Comput. Appl.* **2017**, *28*, 1503–1513. [[CrossRef](#)]
23. Pan, Z.Y.; Cui, W.C.; Miao, Q.M. Numerical simulation of vortex-induced vibration of a circular cylinder at low mass-damping using RANS code. *J. Fluids Struct.* **2007**, *23*, 23–37. [[CrossRef](#)]
24. Khalak, A.; Williamson, C.H.K. Fluid forces and dynamics of hydroelastic structure with very low mass and damping. *J. Fluids Struct.* **1997**, *11*, 937–982. [[CrossRef](#)]
25. Prasanth, T.K.; Mittal, S. Vortex-induced vibration of two circular cylinders at low Reynolds number. *J. Fluids Struct.* **2009**, *25*, 731–741. [[CrossRef](#)]
26. Papaioannou, G.V.; Yue, D.K.P.; Triantafyllou, M.S.; Karniadakis, G.E. On the effect of spacing on the vortex induced vibrations of two tandem cylinders. *J. Fluids Struct.* **2008**, *24*, 833–854. [[CrossRef](#)]
27. Khalak, A.; Williamson, C.H.K. Dynamics of a hydroelastic cylinder with very low and damping. *J. Fluids Struct.* **1996**, *10*, 455–472. [[CrossRef](#)]
28. Sankar, P.S.; Prasad, R.K. Process modeling and particle flow simulation of sand separation in cyclone separator. *J. Part. Sci. Technol.* **2015**, *33*, 385–392. [[CrossRef](#)]
29. Sun, X.; Kim, S.; Yang, S.D.; Kim, H.S.; Yoon, J.Y. Multi-objective optimization of a Stairmand cyclone separator using Response Surface Methodology and computational fluid dynamics. *J. Powder Technol.* **2017**, *320*, 51–65. [[CrossRef](#)]
30. Rahmani, S.; Mousavi, S.M.; Kamali, M.J. Modeling of road-traffic noise with the use of genetic algorithm. *J. Appl. Soft Comput.* **2011**, *11*, 1008–1013. [[CrossRef](#)]
31. Deb, K.; Pratap, A.; Agarwal, S.; Meyarivan, T. A fast and elitist multi-objective genetic algorithm: NSGA-II. *J. IEEE Trans. Evol. Comput.* **2002**, *6*, 182–197. [[CrossRef](#)]
32. Wang, B.; Xu, D.L.; Chu, K.W.; Yu, A.B. Numerical study of gas-solid flow in a cyclone separator. *J. Appl. Math. Model.* **2006**, *30*, 1326–1342. [[CrossRef](#)]
33. Sakamoto, H.; Haniu, H. Optimum suppression of fluid forces acting on a circular cylinder. *J. Fluids Eng.* **1994**, *116*, 221–227. [[CrossRef](#)]
34. Zhao, M.; Cheng, L.; Teng, B.; Liang, D.F. Numerical simulation of viscous flow past two circular cylinders of different diameters. *Appl. Ocean. Res.* **2005**, *27*, 39–55. [[CrossRef](#)]
35. Morse, T.L.; Williamson, C.H.K. Fluid forcing, wake modes, and transitions for a cylinder undergoing controlled oscillations. *J. Fluid Struct.* **2009**, *25*, 617–712. [[CrossRef](#)]